Nuclear Inst, and Methods in Physics Research B 415 (2018) 127–135

Contents lists available at ScienceDirect

Nuclear Inst. and Methods in Physics Research B

journal homepage: www.elsevier.com/locate/nimb

A ballistic transport model for electronic excitation following particle impact

S. Hanke, C. Heuser, B. Weidtmann*, A. Wucher

Fakultät für Physik, Universität Duisburg-Essen, D-47048 Duisburg, Germany

ARTICLE INFO

Keywords:
Ballistic transport
Boltzmann equation
Electronic excitation

ABSTRACT

We present a ballistic model for the transport of electronic excitation energy induced by keV particle bombardment onto a solid surface. Starting from a free electron gas model, the Boltzmann transport equation (BTE) is employed to follow the evolution of the temporal and spatial distribution function $f(\vec{r},\vec{k},t)$ describing the occupation probability of an electronic state $\vec{k}$ at position $\vec{r}$ and time t. Three different initializations of the distribution function are considered: i) a thermal distribution function with a locally and temporally elevated electron temperature, ii) a peak excitation at a specific energy above the Fermi level with a quasi-isotropic distribution in k-space and iii) an anisotropic peak excitation with k-vectors oriented in a specific transport direction. While the first initialization resembles a distribution function which may, for instance, result from electronic friction of moving atoms within an ion induced collision cascade, the peak excitation can in principle result from an autoionization process after excitation in close binary collisions. By numerically solving the BTE, we study the electronic energy exchange along a one dimensional transport direction to obtain a time and space resolved excitation energy distribution function, which is then analyzed in view of general transport characteristics of the chosen model system.

1. Introduction

The excitation of the electronic degrees of freedom following the impact of a keV particle onto a solid surface manifests in three different experimentally accessible observables: the formation of secondary ions within the flux of particles released ("sputtered") from the surface [1], the emission of electrons into the vacuum ("external" electron emission) [2,3] and the flux of excited charge carriers through a buried internal energy barrier realized, for instance, by the insulating film of a metal-insulator–metal junction ("internal" electron emission) [4]. In order to understand the results of such measurements and arrive at a prediction of those quantities, we proposed a model to calculate the excitation of electronic degrees of freedom resulting from electronic friction of moving particles and autoionization following close binary collisions in a particle impact-induced atomic collision cascade [5–7]. As one of the essential ingredients of such a model, the rapid transport of excitation energy away from the spot of its generation was described in terms of a diffusive approach involving a nonlinear diffusion equation, where the electron energy diffusivity was coupled to the local and temporal lattice disorder, yielding a four-dimensional excitation energy density profile which may then be parametrized in terms of an elevated time and position dependent electron temperature. The resulting electron temperature profiles were then employed to obtain external electron emission yields by means of a slightly modified Richardson-Dushman approach [8,9] or to assign ionization probabilities to each sputtered atom according to the so-called substrate excitation model [10].

In contrast to the rather successful calculation of *external* electron yields, a straightforward adoption of the thermionic emission approach to calculate *internal* electron emission yields turned out to give results underestimating experimental data by orders of magnitude [11]. This discrepancy may be explained in terms of the large electron mean free paths within the first femtoseconds after the projectile impact. Thus, the applicability of the diffusion model must be put into question especially at that particular time interval, which coincides with the period where most of the (internal and external) electron emission is assumed to take place.

Therefore, it was concluded that the ballistic nature of the transport process probably has to be taken into account within the model. One attempt was done in terms of a hybrid model [12] combining diffusive and ballistic transport of the excited electrons. First, for a set of layers in different depths below the surface, electron temperatures are calculated according to the standard diffusion model. Then, each layer is regarded as a source of hot electrons according to the Richardson-Dushman

* Corresponding author.
E-mail address: boris.weidtmann@uni-due.de (B. Weidtmann).

https://doi.org/10.1016/j.nimb.2017.11.018
Received 6 September 2017; Received in revised form 15 November 2017; Accepted 16 November 2017

model. These hot electrons are now assumed to undergo a ballistic transport, which is phenomenologically described via an effective mean free path λ for inelastic energy losses preventing them from being able to traverse the buried tunneling barrier. Depending on the traveling length x towards the barrier, the probability to arrive at the metal–insulator interface and contribute to the internal emission yield is then described by $\exp(-x/\lambda)$. With this approach, it was shown that the calculated internal electron emission yields are of the right order of magnitude as measured experimentally. However, this hybrid model is not capable of treating directional effects as induced, for instance, via a variation of the projectile angle of incidence, arising from the extremely anisotropic excitation spectra found in [13].

In order to tackle this problem and take the treatment of electronic excitation transport one step further, the present work employs the classical Boltzmann transport equation (BTE) enabling a more fundamental investigation of the ballistic transport characteristics of electronic excitation energy generated in the first few femtoseconds after the projectile impact. Different initial distribution functions $f(\vec{r},\vec{k},t=0)$ for the occupation probability density of an electronic state with wave number $\vec{k}$ at position $\vec{r}$ and time t are implemented representing different excitation mechanisms such as electronic friction (generating a thermal-like distribution [14–17] and electron promotion (generating single electron excitations above the Fermi level [7,18]). The latter, which in the following will be referred to as "'peak excitation"', is considered to model the fate of a single electron excitation and investigate the competition between ballistic transport and thermalization via electron–electron scattering. The temporal and spatial evolution of the distribution function $f(\vec{r},\vec{k},t)$ obtained this way can be analyzed with respect to the transport of excitation energy, and the results will be compared to the formerly used diffusive transport model.

2. Model

Once excitation energy has been generated within an atomic collision cascade, we can model its dynamics by means of the Boltzmann transport equation (BTE)

$$\left[\frac{\partial}{\partial t}+\frac{\hbar\vec{k}}{m_e}\cdot\nabla_{\vec{r}}\right]f(\vec{r},\vec{k},t)=\left.\frac{\partial f}{\partial t}\right|_{e-e}. \tag{1}$$

for the distribution function $f(\vec{r},\vec{k},t)$ describing the occupation probability density of an electronic state with wave vector $\vec{k}$. The left hand side of Eq. (1) represents the variation of $f(\vec{r},\vec{k},t)$ in space and time due to ballistic transport, whereas the right hand side of Eq. (1) takes into account the changes of the distribution function due to electron–electron scattering. Note that electron phonon collisions are neglected here, since the relevant timescale for these interactions is of the order of picoseconds [19], whereas the typical timescale of electron emission which is targeted here is only a few femtoseconds [8,9].

In detail, the variation of f due to electron–electron scattering, where electrons with initial wave vectors $\vec{k}$ and $\vec{k}_1$ are scattered into states with wave vectors $\vec{k}_2$ and $\vec{k}_3$ and vice versa, is given by

$$\begin{aligned}\left.\frac{\partial f}{\partial t}\right|_{e-e}=&\frac{2\pi\Omega^2}{\hbar}\int_\Omega d^2k_1\int_\Omega d^2k\ \ |M_{ee}(\Delta k)|^2\delta(\epsilon(\vec{k})+\epsilon(\vec{k}_1)-\epsilon(\vec{k}_2)\\&-\epsilon(\vec{k}_3))\times[f(\vec{k}_2)f(\vec{k}_3)(1-f(\vec{k}))(1-f(\vec{k}_1))\\&-f(\vec{k})f(\vec{k}_1)(1-f(\vec{k}_2))(1-f(\vec{k}_3))].\end{aligned} \tag{2}$$

In Eq. (2), M_{ee} denotes the electron–electron scattering matrix element in the k-space and Ω is the volume of an individual discretization cell. The essential physical input entering M_{ee} is the Fourier transform of a screened Coulomb electron–electron interaction potential

$$V(\vec{r})=\frac{e^2}{4\pi\,\epsilon_0\,r}e^{-\kappa r}. \tag{3}$$

with κ denoting the characteristic inverse screening length as the only free parameter of the model. For simplicity, we use the Thomas–Fermi screening length [20]

$$\kappa_{TF}=\frac{2\cdot m_e\cdot e^2}{\epsilon_0\,\hbar^2}\left(1-\exp\left(-\frac{\hbar^2\pi n}{m_e k_B T_e}\right)\right) \tag{4}$$

yielding $\kappa = 3.6\ \text{Å}^{-1}$ for the electron density n given below. A more sophisticated determination of the screening length would be a self consistent calculation of this quantity according to the equation

$$\kappa^2=\frac{e^2 m_e}{\pi^2\hbar^2\,\epsilon_0}\int_0^\infty dk\ f\left(k,t\right). \tag{5}$$

We checked the influence of κ on the calculated diffusion coefficient D (see below) in a range of $[2\ \text{Å}^{-1},5\ \text{Å}^{-1}]$ and find diffusion coefficients varying from 14.7 to 15.3 cm^2/s, indicating a rather weak influence with regard to the goal of the present work.

Using a plane wave approach for the electrons we obtain

$$M_{ee}=\frac{e^2}{2\Omega\,\epsilon_0}\frac{1}{\sqrt{(\Delta k)^2+\kappa^2}} \tag{6}$$

with $\Delta\vec{k}=\vec{k}_1-\vec{k}_2=\vec{k}_3-\vec{k}$ denoting the transfer of momentum between the electrons.

The delta-function $\delta(\epsilon(\vec{k})+\epsilon(\vec{k}_1)-\epsilon(\vec{k}_2)-\epsilon(\vec{k}_3))$ entering Eq. (2) ensures that in the sum over all mathematically possible collisions only those collisions are considered, which are in accordance with energy conservation. In addition, according to Pauli's principle the transition from an initial electronic state with wave vector $\vec{k}_i$ to a different final electronic state with wave-vector $\vec{k}_f$ scales with the probability that the initial state is occupied and the final state is unoccupied, leading to an additional factor $f(\vec{k}_i)(1-f(\vec{k}_f))$.

The numerical integration of this six-dimensional Boltzmann equation turns out to be computationally too expensive. Therefore, we restrict our calculations to one dimension in real space and two dimensions in the k-space, where one direction of the k-space is oriented along the transport direction in real space (x-axis) and the other direction is perpendicular to the transport direction. Note that this refers to a two-dimensional treatment in k-space, and therefore the characteristics of a two-dimensional electron gas need to be used in order to describe the ground state properties of the electronic system. The real space is discretized in cells of length $\Delta x = 3$ Å in the space domain, and the k-space is discretized into 61×61 k-vectors per spatial cell with $\Delta k = 0.054\ \text{Å}^{-1}$. This discretization is a trade-off between cpu-power and the resolution of the k-space. Note that Δk is small compared to the inverse screening length $\kappa = 3.6\ \text{Å}^{-1}$ of the screened Coulomb potential. Due to the finite spacing of the k-grid, fluctuations of the totatl energy in the system may occur. We have therefore repeated a few calculations using a finer spacing and found no significant differences with respect to the presented results.

The ground state properties of the system were set to describe a generic two-dimensional electron gas with a Fermi energy of $E_F = 5.0$ eV, corresponding to an electron density of $n = 2.1\times10^{19}\ \text{m}^{-2}$ and a wave vector $k_F = 1.2\ \text{Å}^{-1}$, which are approximately characteristic for silver at temperature $T = 0$ K. In order to describe a localized excitation of the system, two types of initial conditions for the distribution function $f(\vec{r},\vec{k},t)$ are implemented at a particular point in real space, namely i) a Fermi–Dirac-distribution at different elevated electron temperatures and ii) a 0 K Fermi–Dirac distribution additionally exhibiting one or more non-thermal single electron excitations in terms of selected k-states occupied above E_F.

3. Results

The x-axis was discretized into 35 cells indexed with numbers from 1 to 35. In order to minimize the influence of boundary conditions at both ends of the cell array, the excitation energy was fed into the center of the array at cell #18. In all other cells a ground state distribution function at $T = 0$ K was initialized. The Boltzmann equation was solved numerically using a time step of 0.01 fs. This timestep meets two conditions necessary to ensure the numerical stability of the Boltzmann equation by preventing the complete depopulation of states during a single timestep, namely i) $\Delta t < \frac{\Delta x}{|v_{max}|}$ and ii) $\Delta t \left|\frac{df}{dt}\right| < f$. It should be noted at this point, that the small timestep required by these conditions may not be long enough to ensure that an electron–electron scattering event is completed within one single timestep. Therefore, the Markov chain approximation which forms the basis for the validity of the Boltzmann equation might in principle be violated. Moreover, the time-energy uncertainty precludes the exact energy conversation during one timestep. Both points question the collision integral as calculated by Eq. (2). There is, however, no easy way to improve these points within the classical Boltzmann equation formalism used here.

In detail, the following different initial excitation distributions have been studied:

- six thermal excitations with electron temperatures between 3000 and 20,000 K,
- six isotropic peak excitations with peak energies between 6.0 and 8.5 eV,
- three peak excitations with *k*-vectors preferentially orientated along the transport direction
- three peak excitations with *k*-vectors preferentially orientated perpendicular to the transport direction

3.1. Thermal excitation

In the following, a thermal excitation energy distribution as assumed, for instance, to result from electronic friction processes will be investigated. Therefore, a hot Fermi distribution which can be seen in Fig. 1 was initialized in cell #18, while the system was assumed to be in its ground state with $T = 0$ K in all other cells at the start of the simulation. The evolution of the distribution function is then calculated by Eq. (1) with reflecting boundary conditions set at the two ends of the cell array. To obtain the starting excitation energy contained in cell #18 at $t = 0$, the total energy density of an electron gas at temperature T

$$u(T) = \frac{1}{\pi}\frac{m_e}{\hbar^2}(k_B T)^2 F_{FD}^1\left(\frac{\mu}{k_B T}\right)$$

was calculated with the (two-dimensional) chemical potential μ given by

$$\frac{\mu(n,T_e)}{k_B T_e} = \ln\left(\exp\left(\frac{\hbar^2 \pi n}{m_e k_B T_e}\right) - 1\right). \tag{7}$$

Here, $F_{FD}^1(\eta)$ is the Fermi–Dirac Integral

$$F_{FD}^n(\eta) = \int_0^\infty dx \frac{x^n}{\exp(x-\eta)+1}.$$

In order to obtain the excitation energy, one has to subtract the ground state energy density

$$u_0 = \frac{1}{2\pi}\frac{m_e}{\hbar^2}E_F^2$$

and multiply the difference by the cell volume $\Omega = (3\ \text{Å})^2$. For a specific temperature of 7000 K, this results in a total excitation energy of 1.45 eV, which at $t = 0$ is exclusively located in cell #18 and will in the following be referred to as E_{exc}^0. The excitation energy distribution at later times is then obtained by calculating the energy exchange between neighboring cells as determined by the time evolution of the distribution function *f*. In order to obtain the energy exchange of one cell with its neighboring cells the product $(f(x,\vec{k},t) - f(x,\vec{k},t-\Delta t))E(\vec{k})$ is integrated numerically over all $\vec{k}$.

The time dependent excitation energy distribution calculated this way will then be analyzed in view of the energy transport characteristics. In Fig. 2, this distribution is plotted versus depth at times $t = 0.2$, 0.6, 1.0, 1.4 and 1.8 fs after the start of the simulation, respectively. In this and all following similar plots, the excitation energy contained in a specific cell is normalized to the initial value E_{exc}^0 that was originally fed into the central cell at $x = 51$ Å. At about $t = 2$ fs, the fastest electrons reach the end of the cell array and would be reflected back into the array. To avoid effects of the reflective boundary conditions, the

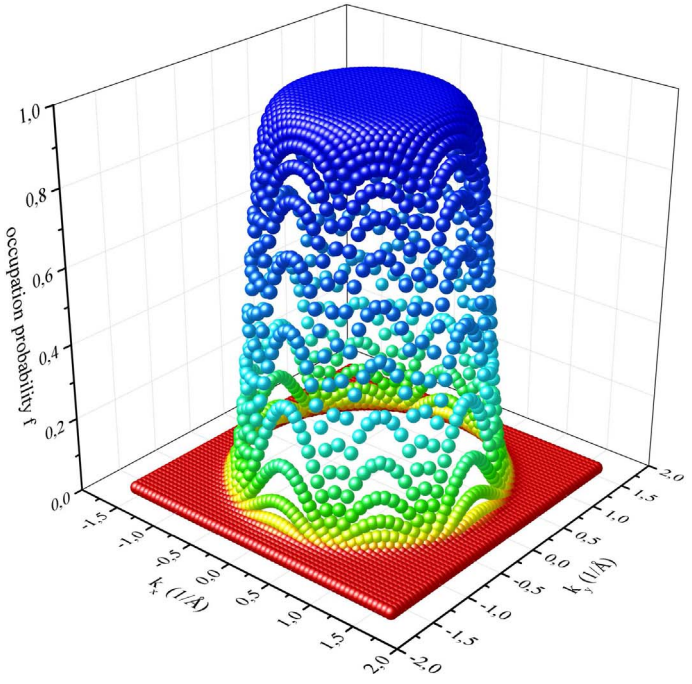

Fig. 1. Occupation probability versus the two-dimensional *k*-vector components k_x and k_y for a hot electron gas at $T = 7000$ K, which is taken as the initial excitation distribution at a depth of 51 Å.

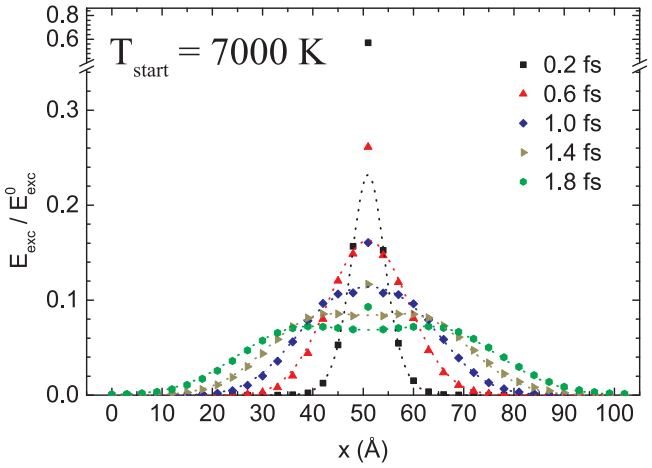

Fig. 2. Excitation energy contained in different cells versus cell depth x for different timesteps. The data were normalized to the initial excitation energy fed into the central cell at $t = 0$ and $x = 51$ Å. The lines represent a three-gaussian fit to the data as explained in the text. Note, that data points at $x = 51$ Å have been excluded from the numerical fitprozedure.

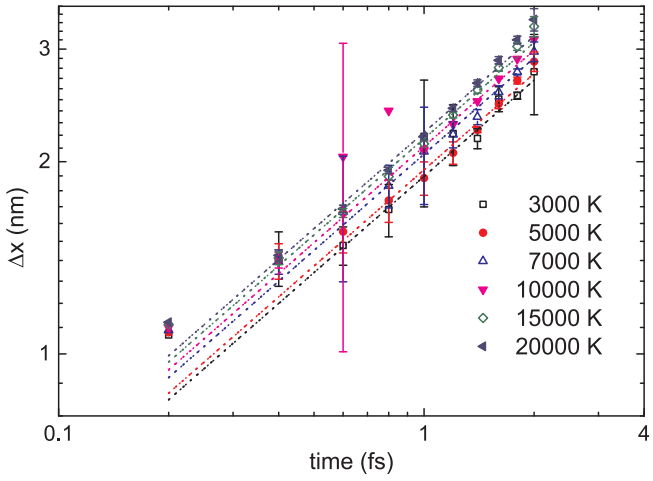

Fig. 3. Width w_{out} of the outer peaks as given from the triple-gaussian fits to the data shown in Fig. 2 plotted vs time for several electron temperatures in the initial cell. Dotted lines: linear fits to the data with a fixed slope of 0.5. The errors bars are obtained from the standard deviation of the fitting parameter w_{out} (the Eq. (8) and following text) as given by the fitting function.

simulation is therefore limited to 1.8 fs. At $t = 0$, there is one δ-like peak at 51 Å, reflecting the local excitation in the central cell, which exhibits a fast decrease with increasing simulation time and broadens during the first femtosecond to a width of approximately 34 Å. After 1.4 fs, the peak is observed to separate into two peaks, with one peak moving left and one peak moving right. We assume that the shifting of these peaks reflects the ballistic transport characteristics, whereas the broadening of the peaks is partly a result of the collisions between the electrons and partly caused by a dispersion effect due to the different components of the initial k-vectors in the transport direction. The peak in the center is due to the k-vectors which are preferrably oriented perpendicular to the transport direction. As the collisions are responsible for diffusive behavior and diffusion would lead to a gaussian distribution of the excitation energy, the data are fitted by a three-gaussian fitting curve:

$$E_{exc}(x) = A_l \cdot \exp\left(-0.5 \cdot \left(\frac{x-(x_c + a \cdot x_0)}{w_l}\right)^2\right) + A_m \cdot \exp\left(-0.5 \cdot \left(\frac{x-(x_c + b \cdot x_0)}{w_m}\right)^2\right) + A_r \cdot \exp\left(-0.5 \cdot \left(\frac{x-(x_c + c \cdot x_0)}{w_r}\right)^2\right) \quad (8)$$

This fit function has ten fitting parameters: A_l,A_r,A_m,w_l,w_m,w_r,x_0,a,b and c, thus giving many combinations of values which all describe the data comparably well. In order to reduce the number of parameters, a few symmetry arguments need to be considered. The symmetry of the initial distribution function does not prefer any direction (left or right), which means that the broadening (represented by the parameters w_l and w_r), the height (represented by A_l and A_r and the shift (represented by the parameters a,c and x_0) of the peaks moving left and right should be same, yielding to $w_l = w_r = w_{out}$, $A_l = A_r$ and $a = -c$. The same symmetry argument may be employed to set the parameter $b = 0$. Assuming a constant velocity for the shifting of the peaks (an assumption which will be examined later), the shift x_0 may be interpolated from the excitation energy profile at the timesteps of 0.2 fs and 1.8 fs. With these assumptions, the number of free parameters can be reduced and a reliable fit becomes possible. The resulting fitting curves are shown as dotted lines in Fig. 2. The central data point at $x = 51$ Å represents the remainder of the initial δ-peak and is caused by electrons with initial k-vectors pointing perpendicular to the transport direction, which have not undergone any scattering with other electrons yet and therefore cannot contribute to energy transport in the x-direction. This data point, which clearly falls out of the observed gaussian peaks, was therefore excluded from the fits. From w_{out}, the half width Δx can be evaluated by $\Delta x = 2\sqrt{2 \cdot \ln(2)} \cdot w_{out}$. In Fig. 3, the width Δx obtained this way is plotted versus time in a double logarithmic manner for different initial excitation temperatures.

For a purely diffusive transport, the width should satisfy the equation

$$(\Delta x)^2 = 2D \cdot t \quad (9)$$

yielding a slope of 1/2 in a double logarithmic plot of Δx vs. t.

Therefore, linear fits were performed to the data displayed in Fig. 3, yielding the slopes listed in Table 1. It is seen that the obtained values exhibit rather good agreement with the diffusive prediction of 0.5. It should be stressed at this point, however, that this does not imply a real diffusive transport, which would require many electron–electron collisions as a necessary prerequisite, but rather constitutes the observation that the mixed dispersive and collision induced spread of excitation calculated by the BTE can at least phenomenologically be treated in terms of a diffusion equation.

From the intercept with the vertical axis at $t = t_0$, a value of the apparent diffusivity D that should be used in such an approximative treatment can be estimated. In order to arrive at more realistic values, additional fits were performed where the slope was fixed to 0.5. the resulting fit curves are indicated as dotted lines in Fig. 3. The resulting "apparent diffusivity" extracted from these fits is shown as a function of temperature in Fig. 4. The first observation is that the apparent diffusion coefficient obtained this way, ranging between $D = 17\ \mathrm{cm}^2/\mathrm{s}$ and $D = 25\ \mathrm{cm}^2/\mathrm{s}$, is of the same order as the value of $D = 20\ \mathrm{cm}^2/\mathrm{s}$ that was used in our earlier work employing the diffusive transport model [6]. Second, it is found that the apparent diffusivity slightly increases with increasing electron temperature of the initial excitation. This finding may be rationalized in terms of

Table 1
Slopes obtained from fits to the data in Fig. 3.

Inital Temperature (K)	Slope
3000	0.45
5000	0.52
7000	0.47
10000	0.51
15000	0.53
20000	0.54

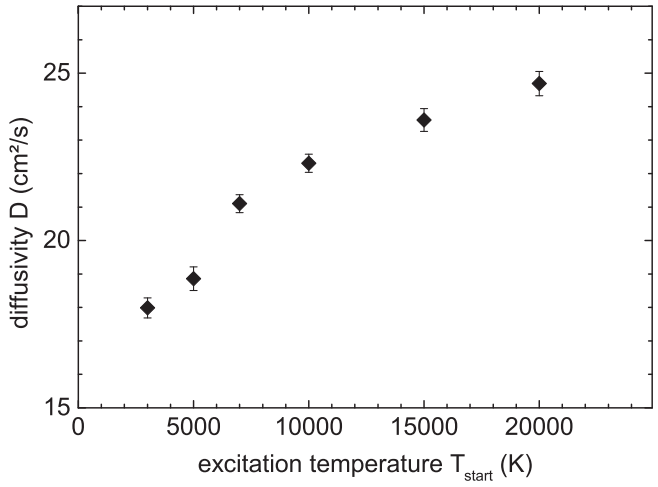

Fig. 4. Apparent diffusivities estimated from the broadening of the excitation energy vs. depth spectra as a function of the initial excitation temperature.

- higher average energy of the excited electrons associated with higher velocities
- larger velocity difference between slowest and fastest electrons leading to stronger dispersion.
- higher electron–electron scattering rate since more *k*-vectors are available for collisions.

3.2. Isotropic peak excitation

In these calculations, the excitation was equally distributed over all available *k*-states with energies in a small range $\Delta E = 0.02$ eV around a specific electron energy *E*. Six peak energies of E=6.0, 6.5, 7.0, 7.5, 8.0 and 8.5 eV were chosen, which correspond to excitation states with excess energies between 1.0 and 3.5 eV above the Fermi level. Ideally, one would want to include a large number of *k*-vectors with the same absolute value but randomly oriented directions in order to describe a truly isotropic excitation. Due to the discretization of the *k*-lattice, however, only specific *k*-vectors are allowed within the energy range ΔE around *E*. Thus, the resulting *k*-distributions are not completely isotropic, and possible directions of *k*-vectors belonging to occupied states depend on the chosen energy *E*. The resulting occupation characteristics will in the following be referred to as “quasi-isotropic” and are shown in Fig. 5.

It is seen that the initial configuration for excitation at 6.0, 6.5 and 7.0 eV clearly differs from that at 7.5, 8.0 and 8.5 eV, respectively. For 6 to 7 eV, all of the occupied *k*-vectors are oriented nearly diagonal to the transport direction, whereas for 7.5 to 8.5 eV half of the occupied *k*-vectors are orientated rather perpendicular and parallel to *x*-axis. To

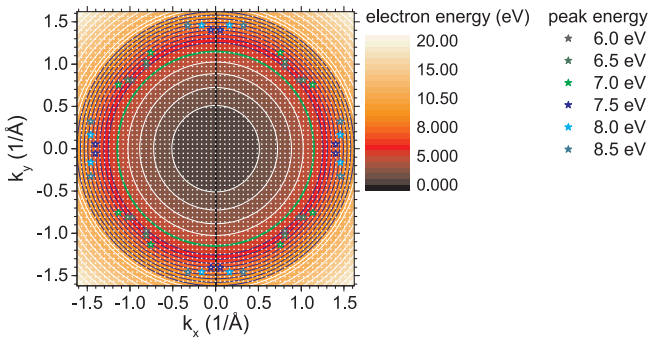

Fig. 5. Quasi-isotropic start distribution of *k*-vectors for peak excitations with different electron energies. Up to an energy of 5 eV (Fermi level, marked with green line), all states are fully occupied, for energies above 5 eV, just the states marked with a star are partly occupied with $f = 0.125$.

calculate the total excitation energy density corresponding to the start configuration, just the states above the Fermi level have to be considered by multiplying the different occupation numbers with the corresponding energy. For the following timesteps, the excitation energy spread is again calculated from the modification of the distribution function *f*.

The resulting excitation energy profile is shown as a function of time in Fig. 6 for an initial peak excitation at 6.0 and 7.5 eV, respectively. At 0.8 fs after a 6 eV excitation, one finds that the energy profile is not centered anymore, but has spread into two symmetrically shaped peaks moving away from the original point of excitation. In case of the 7.5 eV excitation, on the other hand, the distribution remains centered around the initial spot of excitation. Although not shown, we note that the profiles calculated for 6.5 and 7 eV excitation resemble that displayed in Fig. 6a, while the ones calculated for 8.0 and 8.5 eV are similar to the profile displayed in Fig. 6b. The strong decay of the energy density at the point of the initial excitation which is observed in Fig. 6 can be rationalized in terms of the direction of the inital *k*-vectors belonging to the start configuration as displayed in Fig. 5. In the context of the dispersive ballistic energy transport, the important quantity is the k_x-component of an excited electron’s *k*-vector along the transport direction. For 7.5 eV, 8.0 eV and 8.5 eV excitation, there are electrons with initial *k*-vectors featuring k_x-components close to zero. These electrons can only contribute to the energy transport along the *x*-direction via collisions with other electrons, thereby generating the centered peak visible in the distribution of Fig. 6b. Those *k*-vectors which are essentially oriented *along* the transport direction, on the other hand, generate the two additional peaks moving away from the original point of excitation, which are clearly visible both in Fig. 6a and b. For the lower energy excitations, all excited electrons start with a considerable k_x-component along the transport direction, so that the central peak is missing in Fig. 6a.

Again, three gaussian functions are fitted to the excitation profiles as indicated by the dotted lines, with the goal to obtain the width of the peaks moving away from the spot of initial excitation. The obtained widths are shown as a function of time in Fig. 7. For 7.5–8.5 eV excitation, the widths again follow the $\sqrt{t}$ dependence given by Eq. 9. For 6.0–7.0 eV excitation, on the other hand, the broadening of the widths does not follow the time-dependence typical for diffusive transport very well. In addition, the uncertainty is extremely high especially in the first sub-femtosecond regime after the initialization, as the peaks in the plot are not really separable from each other.

Straight line fits to these data yield the slope values listed in Table 2, which exhibit a larger scatter but are still centered around the value of 0.5 as predicted by Eq. 9. Fitting linear curves to the data with a fixed slope of 0.5, the obtained intersections with the $t/t_0 = 1$ axis are used to calculate diffusivities as described above. The resulting values are shown in Fig. 8.

Noticeable is the rise from about 10.6 to 15.2 cm^2/s between 6 and 7 eV excitation, in contrast to the decrease from 27.6 to 24.8 cm^2/s from 7.5 to 8.5 eV excitation. Particularly the jump between the two groups clearly shows the strong effect of the different symmetry of the initial *k*-vector distribution onto the calculated excitation energy transport characteristics.

3.3. Anisotropic excitations

In order to get a better insight into the influence of the primary *k*-vector orientation, the calculations were repeated for a completely anisotropic excitation distribution, which was realized in form of two different initial *k*-vector distributions. First, eight initial *k*-vectors were orientated nearly perpendicular to the *x*-axis (green points in Fig. 9), where the k_x component is close to zero and therefore both the ballistic transport along this axis as well as dispersive broadening should be greatly reduced. In the second case, all excited *k*-vectors were orientated nearly along the *x*-axis (blue points in Fig. 9), thereby fully

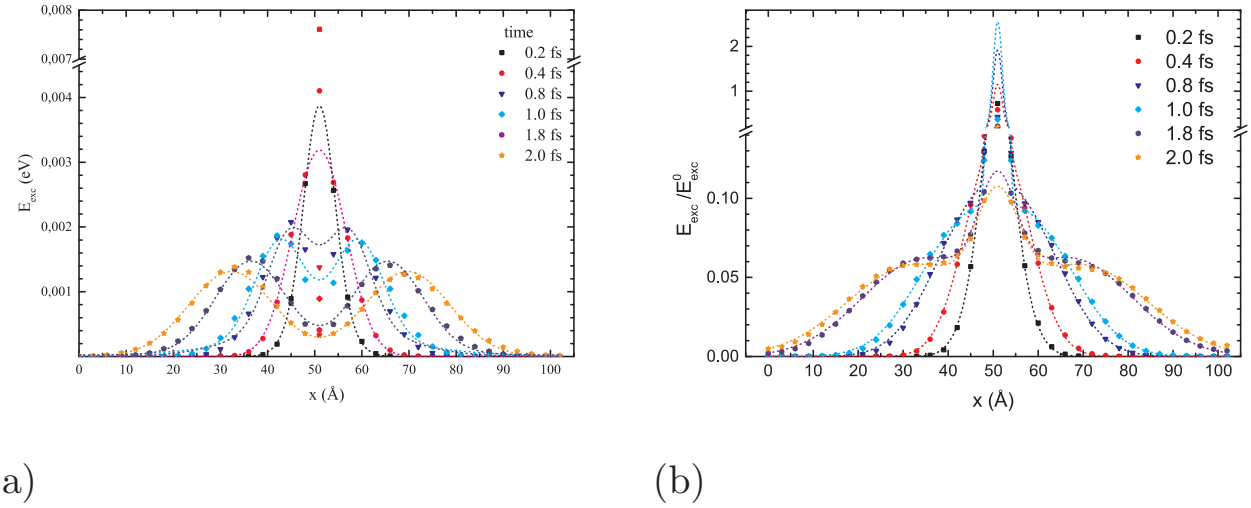

Fig. 6. Excitation energy contained in different cells versus cell depth x for different times after a quasi-isotropic peak excitation at $E = 6$ eV (a) and $E = 7.5$ eV (b). The data were normalized to the initial excitation energy fed into the central cell at $t = 0$ and $x = 51$ Å. The lines represent a three-gaussian fit to the data as explained in the text.

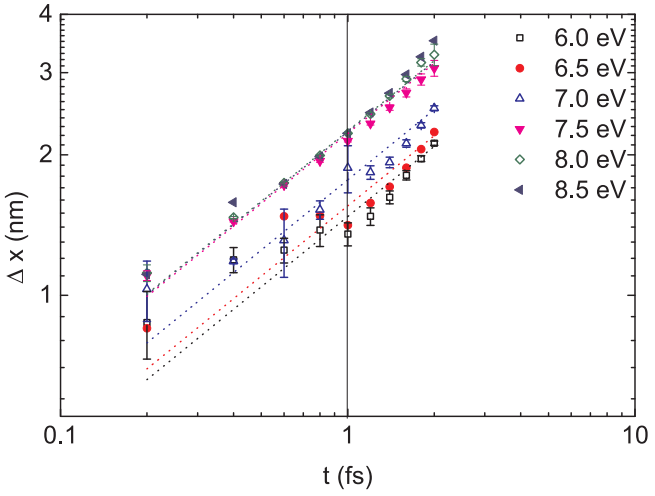

Fig. 7. Half widths of the outer peaks in the excitation profile plotted versus the time for the different initial excitation energies. Again, the error bars are obtained from the standard deviation of the parameter w_{out} as given by the fitting procedure. The dotted lines represent least square fits to the data with the slope being fixed at 0.5 (see text).

Table 2
Slopes obtained from fits to the data in Fig. 7.

Peak excitation energy (eV)	Slope
6.0	0.36
6.5	0.48
7.0	0.69
7.5	0.47
8.00	0.50
8.5	0.47

contributing to the ballistic transport and dispersion. Both cases were calculated for three different peak excitation energies.

For each case, one characteristic excitation energy profile is shown in Fig. 10a and b, respectively.

In case 1 (Fig. 10a) (initialization perpendicular to the transport direction), the excitation energy profile shows one peak symmetric to the point of the initial excitation, the width of which grows with time. Of note is the fact that already after 0.2 fs there is a small amount of excitation visible at about 12 Å away from the original feeding point, corresponding to a transport velocity of about 60 Å/fs. In comparison, the highest initial k-vector component along the transport direction is about 0.54 $Å^{-1}$, corresponding to a ballistic velocity of 6.26 Å/fs. Obviously, electron–electron collisions take place already during the first 0.2 fs, where electrons are scattered into the transport direction. A careful analysis of the curve plotted for $t = 1.8$ fs reveals that the peak shows a kind of shoulder, which cannot be represented by a single gaussian. This shoulder originates from a rising number of scattered electrons with k_x-components into transport direction, again building one peak moving to the right and one peak moving to the left, respectively. Therefore, the triple gaussian function (Eq. (8)) is again employed to fit the data. The widths obtained that way are plotted in Fig. 11.

Except the point at 0.4 fs obtained for 8 eV excitation, the data can be reasonably fitted by straight lines with the slopes listed in Table 3. Fitting again straight lines with a fixed slope of 0.5, on the other hand, one finds a systematic deviation towards higher slope at larger times. From the corresponding lines indicated in Fig. 11a, however, we can still calculate effective diffusion coefficients which are plotted in Fig. 12.

For case 2 (initialization in transport direction) only one peak can be seen, which moves to the right as expected from the initial k-vectors pointing into the positive x-direction. After 0.8 fs, the peak is no longer symmetric but shows a shoulder at the left side. The existence of excitation energy at $x < 51$ Å(where the original excitation is fed into the system) is clear evidence for the action of electron–electron collisions, as there are initially no excited electrons with a velocity component in the negative x-direction. In order to consider this shoulder, the following two-gaussian fit function was employed:

$$E_{exc}(x) = A_l \cdot \exp\left(-\frac{1}{2}\left(\frac{x-d_l}{w_l}\right)^2\right) + A_r \cdot \exp\left(-\frac{1}{2}\left(\frac{x-d_r}{w_r}\right)^2\right)$$

From the corresponding fits, the widths w_r of the main peaks on the right hand side were determined and are shown in Fig. 11. In the first femtosecond, the slopes for all energies seem to be significantly larger than 0.5, so that no apparent diffusivity can be estimated for this time interval. In fact, a purely ballistic transport of the excited electrons would yield a slope of 1.0, which indeed seems to be closely approximated during the first femtosecond. At later times, however. the data points are better approximated by a linear fit with the slope 0.5, allowing again the determination of effective diffusion coefficients as displayed in Fig. 12. It is seen that the diffusivity values induced by an anisotropic peak excitation again range between 6 and 23 cm^2/s and show a consistent increase with increasing peak energy. Interestingly,

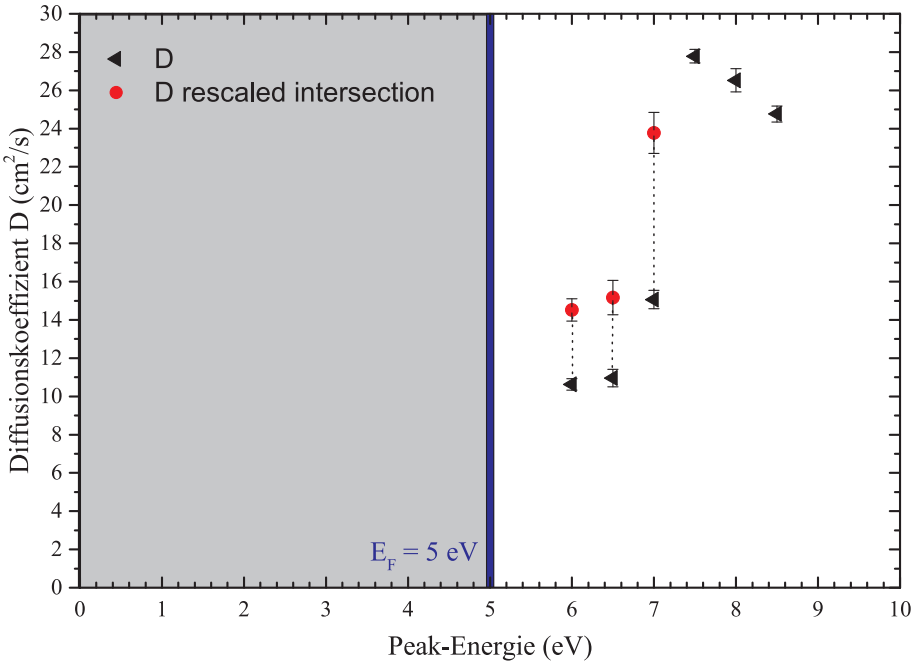

Fig. 8. Diffusivity values obtained from the fit curves displayed in Fig. 7 for quasi-isotropic peak excitation at different peak energies.

the influence of the initial *k*-vector orientation appears to be rather weak. In view of this finding, it is of interest to take a closer look at the drift velocity of the excitation peaks found in Figs. 2, 6 and 10. As an example, we show the position of the peak maxima identified in Fig. 10b as a function of time in Fig. 13.

It is obvious that the excitation is moving through the system with a constant drift velocity, which from the slope of the indicated straight line fit is determined as v_D = 14 Å/fs. Interestingly, this value is found to be essentially independent of the peak excitation energy. In particular, the observed drift velocity does not reflect the initial *k*-vectors of the excited electrons added to the system at t=0, which correspond to electron velocities of 14.5, 15.6 and 16.8 Å/fs at peak energies of 6, 7 and 8 eV, respectively. In contrast, the value appears to correspond nicely with the Fermi velocity v_F = 13.9 Å/fs. If the same analysis is repeated for the data displayed in Figs. 6, 7 and 11, however, one finds drift velocities in the range 6.3…8.5 Å/fs for anisotropic excitation perpendicular to the transport direction and 9.0…10.7 Å/fs for a quasi-isotropic peak excitation. In all cases, the drift velocity does not show any significant dependence on the peak excitation energy outside the experimental error. For thermal excitation, we find drift velocities ranging from 9.5 to 7.3 Å/fs, which exhibit a consistent *decrease* with increasing excitation temperature. Note that all of these values are significantly below the Fermi velocity of the model system employed here. At present, we therefore do not have a simple explanation for the observed drift velocity.

4. Conclusion

We present a microscopic model describing the transport of electronic excitation energy in a generic metallic system via solution of the Boltzmann transport equation. The results show that both the random transport via electron–electron scattering and more directional transport components induced by ballistic motion of excited electrons need to be taken into account to understand the extremely fast transport of a localized excitation away from its original point of generation. These results are important particularly in view of the transient excitation generated by a localized particle impact onto a solid surface. As the only material parameters entering the description are the Fermi energy and the electron density, the model should be applicable to all metals where the assumption of a free electron gas is valid. In these cases,

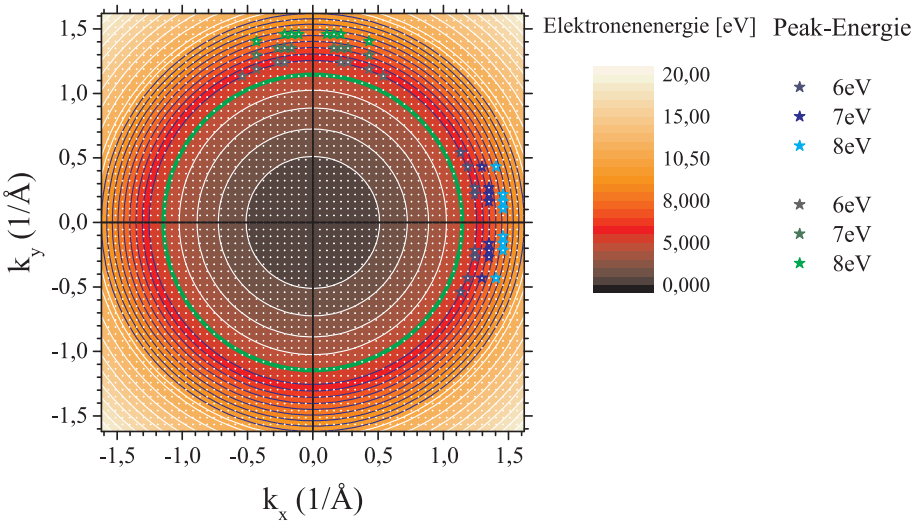

Fig. 9. Initial *k*-vector distributions for anisotropic peak excitation at different peak energies. Up to an energy of 5 eV (Fermi level, marked with green line), all states are fully occupied, for energies above 5 eV, just the states marked with a star are partly occupied with f = 0.125.

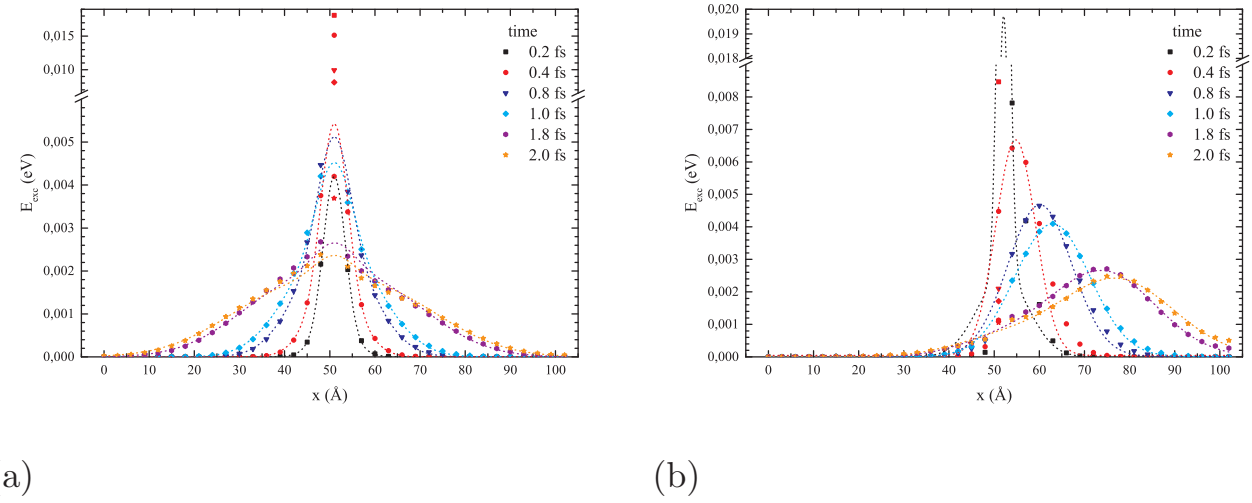

Fig. 10. Excitation energy contained in different cells versus cell depth x for different times after an anisotropic peak excitation at $E = 8$ eV with the initial k-vectors oriented perpendicular to (a) and along (b) the transport direction. The data were normalized to the initial excitation energy fed into the central cell at $t = 0$ and $x = 51$ Å. The lines represent a three-gaussian (a) respectively two gaussian (b) fit to the data as explained in the text.

electronic excitation generated via electronic stopping of either the projectile itself or target atoms recoiling after (elastic or inelastic) collisions with the projectile is originally localized within a distance of only a few Angstroms around the moving particle. The further fate of the bombarded solid then critically depends on the speed at which these excitations are spread in the system. In cases where the electronic excitation remains localized for a long enough time to allow significant nuclear motion, it may, for instance, strongly influence the excitation state of particles released ("sputtered") from the surface as a consequence of a projectile-induced atomic collision cascade. In other cases, it may act to heat the lattice via electron–phonon coupling, thereby leading to so-called "electronic" sputtering even in high energy impact events where the initial energy transfer is completely dominated by electronic excitation. In this context, the electronic transport is so far practically always modeled in terms of a diffusive approach, using the effective diffusivity of the excitation energy as a free fitting parameter. The present data allows to go one step beyond the simple diffusion approach, but is far too computationally expensive to permit a full trace of the electronic excitation within an atomic collision cascade, which typically extends over spatial dimensions of the order of 10 nm and

Table 3
Slopes obtained from fits to the data in Fig. 11.

Peak energy (eV)	Slope
6.0	0.39
7.0	0.42
8.00	0.48

times of several picoseconds. Therefore, the analysis presented here appears helpful since it allows to judge the validity of and error introduced by the diffusive treatment on one hand, but at the same time provides a means to estimate the effective diffusivity parameter which should be introduced into such an approximative model. More specifically, the results obtained here lend more credibility to our previous selection of this parameter, which was based on somewhat shaky arguments involving approximative dependencies of electron mean free paths on parameters like electron and lattice (phonon) temperature, in connection with the assumption of an instantaneously elevated lattice temperature after a projectile impact. In that respect, we feel that the

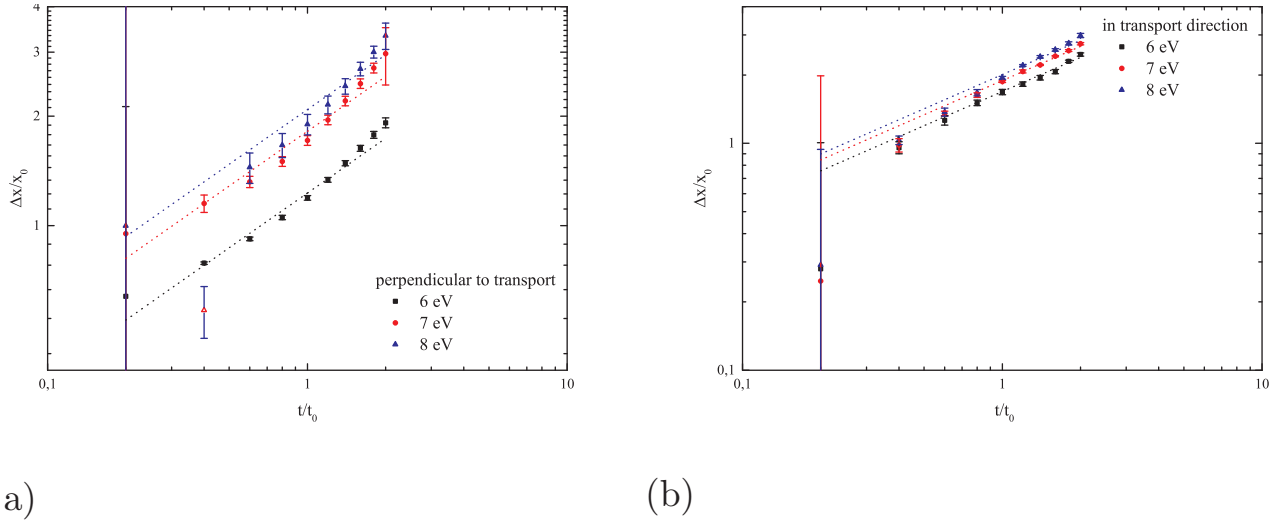

Fig. 11. Widths of the gaussian peaks fitted to the excitation energy profiles in Fig. 10 versus time. x_0 and t_0 are chosen as before. Again, the error bars are obtained from the standard deviation of the parameter w_{out} as given by the fitting procedure.

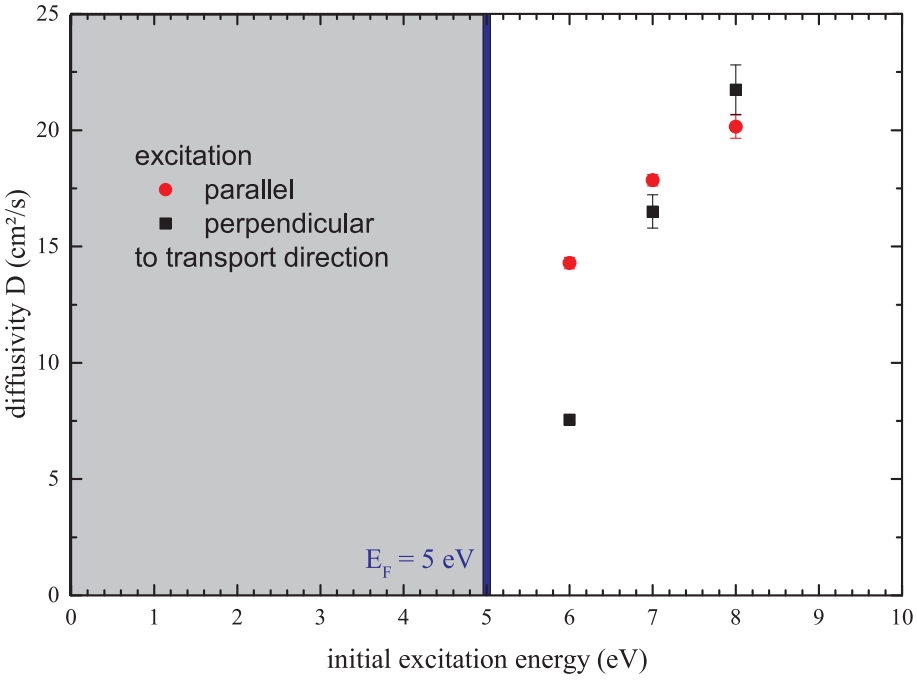

Fig. 12. Effective diffusion coefficients estimated from the excitation energy profile resulting from an anisotropic excited *k*-vector distribution.

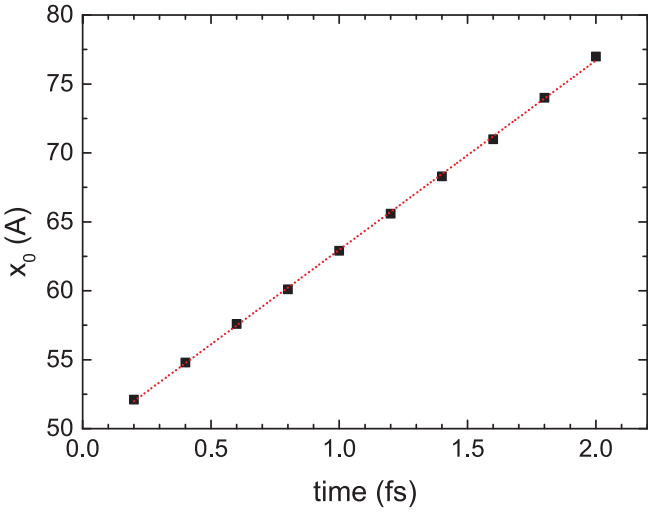

Fig. 13. Position of the peak maximum observed in Fig. 10b vs time.

data obtained here, even for the restricted system that is presently tractable, provide a useful basis for further insights and developments regarding the transport of localized electronic excitations in solids.

Acknowledgements

We thank Baerbel Rethfeld (Technical University Kaiserslautern) and her group as well as Orkhan Osmani and Mourad El-Kharrazi for many fruitful discussions. We would also like to thank the Deutsche Forschungsgemeinschaft for funding in the framework of the Collaborative Research Center (SFB) 616 in the beginning of this project.

References

[1] P. Sigmund, Theory of sputtering. In sputtering yields of amorphous and polycrystalline targets, Phys. Rev. 184 (1969) 383.
[2] J. Ferron, E.V. Alonso, R.A. Baragiola, A. Oliva-Florio, Dependence of ion-electron emission from clean metals on the incidence angle of the projectile, Phys Rev. B 24 (1981) 4412.
[3] G. Falcone, Z. Šroubek, Kinetic electron-emission from solids induced by slow particles, Nucl. Instrum. Methods B 58 (3–4) (1991) 313–316.
[4] D.A. Kovacs, J. Winter, S. Meyer, A. Wucher, D. Diesing, Photo and particle induced transport of excited carriers in thin films tunnel junctions, Phys. Rev. B 76 (2007) 235408.
[5] A. Duvenbeck, O. Weingart, V. Buss, A. Wucher, On the role of electronic friction and electron promotion in kinetic excitation of solids, Nucl. Instrum Methods B 285 (2007) 83.
[6] A. Duvenbeck, A. Wucher, Low-energy electronic exitation in atomic collision cascades: a nonlinear transport model, Phys. Rev. B 72 (2005) 165408.
[7] A. Duvenbeck, O. Weingart, V. Buss, A. Wucher, Electron promotion and electronic friction in atomic collision cascades, New J. Phys. 9 (2007) 38.
[8] A. Duvenbeck, B. Weidtmann, A. Wucher, Predicting kinetic electron emission in molecular dynamics simulations of sputtering, J. Phys. Chem. C 114 (2010) 5715.
[9] A. Duvenbeck, S. Hanke, B. Weidtmann, A. Wucher, A molecular dynamics investigation of kinetic electron emission from silver surfaces under varying angle of projectile impact, Nucl. Instrum. Methods B 269 (2011) 1661.
[10] Z. Šroubek, Formation of ions in sputtering, Spectrochim. Acta B 44 (1988) 317.
[11] S. Hanke, A. Duvenbeck, C. Heuser, B. Weidtmann, D. Diesing, M. Marpe, A. Wucher, Computer simulation of internal electron emission in ion-bombarded metals, Nucl. Instrum. Methods B 303 (2013) 55–58.
[12] S. Hanke, A. Duvenbeck, C. Heuser, B. Weidtmann, A. Wucher, A hybrid model describing ion induced kinetic electron emission, Nucl. Instrum. Methods B 352 (2015) 18–21.
[13] J.I. Juaristi, M. Rösler, Atomic number dependence of the forward/backward kinetic electron emission induced by slow ions in carbon foils, Nucl. Instrum Methods B 157 (1999) 254.
[14] M. Lindenblatt, E. Pehlke, A. Duvenbeck, B. Rethfeld, A. Wucher, Kinetic excitation of solids: the concept of electronic friction, Nucl. Instrum. Methods B 246 (2006) 333.
[15] D. Mason, C. Race, W. Foulkes, A. Horsfield, A. Sutton, Quantum mechanical simulations of electronic stopping in metals, Nuclear. Instrum. Methods B 269 (2011) 1640.
[16] S. Cernusca, A. Diem, H.P. Winter, F. Aumayr, J. Lorincik, Z. Šroubek, Kinetic electron emission from highly oriented pyrolytic graphite surfaces induced by singly charged ions, Nuclear. Instrum. Methods B 193 (2002) 616–620.
[17] Z. Šroubek, G. Falcone, Electronic excitation-spectra and energy losses of slow ions in solids, Phys. Rev. B 39 (1989) 1999.
[18] A. Duvenbeck, B. Weidtmann, O. Weingart, A. Wucher, Modeling hot-electron generation induced by electron promotion in atomic collision cascades in metals, Phys. Rev. B 77 (2008) 245444.
[19] B. Rethfeld, Mikroskopische Prozesse bei der Wechselwirkung von Festkörpern mit Laserpulsen im Subpicosekundenbereich (Ph.D. thesis), Technische Universität Braunschweig, 1999.
[20] H. Haug, S.W. Koch, Quantum Theory of the Optical and Electronic Properties of Semicounductors, fifth ed., World Scientific, 2009.